A wing characterization method for flapping-wing robotic insects

Alexis Lussier Desbiens*, Yufeng Chen*, Robert J. Wood
* Contributed equally to the work

***Abstract*— This paper presents a wing characterization method for insect-scale flapping-wing robots. A quasi-steady model is developed to predict passive wing pitching at mid-stroke. Millimeter scale wings and passive hinges are manufactured using the SCM fabrication processes. Flapping experiments at various frequencies and driving voltages are performed to extract kinematics for comparison with the quasi-steady predictions. These experiments examine the validity of the quasi-steady model and demonstrate the robustness of the wing characterization method. In addition, because time-averaged lift and drag are strongly correlated with flapping kinematics, quasi-steady prediction of wing kinematics directly leads to predictions of lift and drag generation. Given a flapping frequency and a driving voltage, the model computes the hinge stiffness that leads to optimal flapping kinematics. This reduces the number of flapping experiments required for wing characterization by a factor of four.**

I. Introduction

Recent advances in microfabrication and bio-inspired control algorithms led to the first hovering flight of the Harvard RoboBee. In order to achieve fully autonomous flight, a power source, sensors and computational capabilities must be integrated into future designs. These components will contribute substantial added mass, requiring more effective and efficient propulsion.

The current RoboBee design, shown in Figure 1, utilizes bimorph piezoelectric actuators to actively control wing stroke motion, while the wing pitch motion is mediated by a passively rotating hinge. This under-actuated design reduces system mass and complexity and poses challenging control problems. The current RoboBee generates a mean lift of $1.3\mathrm{mN}$ at peak performance, however its mean coefficient of lift is one-third that of real insects [1]. This gap implies a large margin for potential improvement, which requires an understanding of the relevant aerodynamic principles and the development of efficient testing methods.

Dickinson first observed flapping-wing aerodynamic mechanisms such as rotational circulation and delayed stall through studying the dynamics of a scaled up flapping wing model [2]. Ennos proposed the possibility of passive wing rotation through based solely on the wing inertia [3]. Bergou proposed a model of insect wing rotation based on passive wing pitch reversal [4]. To further study passive rotation, Whitney designed the first insect scale flapping wing experiments with a passive hinge [5]. These studies provided insights into wing aerodynamics, yet there is no complete model that predicts wing kinematics and the resulting forces and torques for a given planform and hinge compliance. This paper details the results of extensive experiments to describe wing kinematics with a passive hinge. A quasi-steady model is proposed to predict maximum pitch angle, which is crucial to thrust production. This model is then validated and used to identify optimal kinematics for the Robobee wing.

The authors are with the Harvard Microrobotics Laboratory, Harvard University, Cambridge, MA 02138, USA {desbiens, yufengchen,rjwood}@seas.harvard.edu

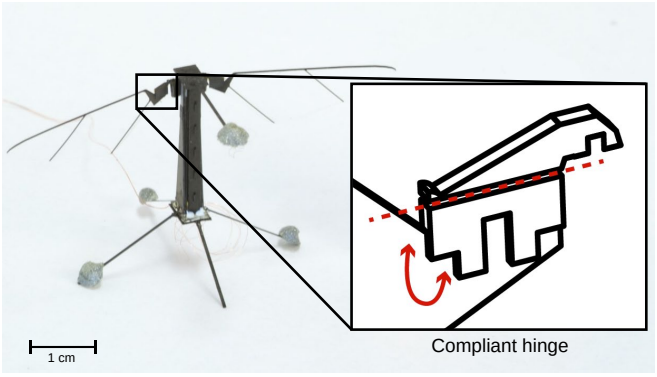

Fig. 1. The RoboBee is an 80mg flapping-wing robotic insect. The stroke is controlled by a bimorph piezoelectric actuator while the pitch joint is passive and made of a compliant Kapton hinge. Image courtesy of Pakpong Chirarattananon.

Experimentally, wing characterization refers to the process of finding the optimal flapping frequency and actuator voltage that lead to desired wing kinematics and lift generation. Throughout this paper, an operating point refers to a specific driving frequency and voltage amplitude pair. Previous brute force characterization methods were tedious because a large number of operating points needed be tested manually. The proposed quasi-steady model is used to develop a wing characterization method that predicts wing kinematics for different driving frequencies, stroke amplitudes, and wing hinge stiffnesses. This method is shown to be robust in predicting kinematic parameters in the large RoboBee operational range. Hence the method greatly reduces the required number of experiments needed to design the hinge joint for optimal performance at a desired operating point.

II. Flight kinematics and quasi-steady modeling of passive rotation

In addition to dependence on morphological parameters, lift and drag of a passively rotating wing is strongly correlated to kinematics. In this paper, the wing motion can be described by two simple rotations, stroke and pitch, as the hinge axis motion ($\hat{x}_S$) is constrained to the $\hat{y}_\mathcal{N} - \hat{x}_\mathcal{N}$ plane

Three reference frames are introduced to describe the wing motion and are illustrated in Figure 2. The first rotation, named stroke, rotates the $\mathcal{S}$ frame around the $\hat{z}_{\mathcal{N}}$ axis of the inertia frame $\mathcal{N}$ by an angle ϕ. This rotation is controlled by the piezoelectric actuator with sinusoidal input , flapping frequency f and maximum stroke amplitude $\phi_{\max}$. The second rotation rotates the frame $\mathcal{H}$, attached to the wing, by an angle ψ around the hinge axis $\hat{x}_{\mathcal{S}}$. This pitch induced passively due to the hinge stiffness, the wing inertial properties and the aerodynamical forces. For the calculations presented in this paper, the pitch motion is approximated as a sinusoid of frequency f and maximum amplitude $\psi_{\max}$ by fitting the experimental measurement. This is a good approximation of the motion measured experimentally, as one can see in Figure 3. Furthermore, due to the passive nature of the wing pitch rotation, a phase offset δ is observed between the stroke reversal ($\dot{\phi} = 0$) and the wing pitch zero-crossing ($\psi = 0$), as illustrated in Figure 3.

The flapping kinematics are split into two phases: translational and rotational, in which lift and drag are generated by different mechanisms as illustrated in Figure 3. The following sections describe these two phases separately and introduce quasi-steady modeling of wing motion and the resulting forces.

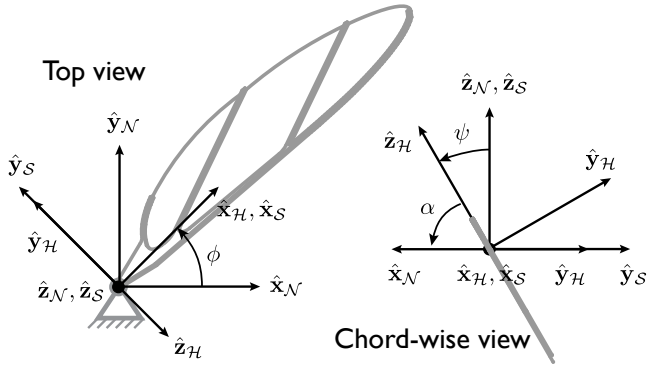

Fig. 2. Coordinate definition and description of wing kinematics. Stroke (ϕ) and pitch (ψ) motion refer to rotation with respect to the $\hat{z}_{\mathcal{N}}$ axis and to the $\hat{x}_{\mathcal{S}}$ axis, respectively. Angle of attack is defined as $\alpha = 90 - \psi$.

A. Rotational phase

The rotational phase occurs during wing pitch reversal at the transition between down and up strokes. During this phase, the wing experiences a large angular acceleration along the spanwise rotational axis. Leading edge vortices detach from the upper surface and new vortices are generated subsequently on the lower surface. Dickinson demonstrated that advanced pitch rotation induces favorable circulation to increase lift and reduce drag [2]. In our experiments, we have observed both advanced and delayed passive rotation. At low flapping frequency (80Hz - 95Hz), wing pitch reversal usually precedes stroke reversal because the hinge restoring torque dominates inertial and aerodynamic contributions. As flapping frequency increases, wing pitch reversal becomes progressively delayed as inertial effects start to dominate the pitching motion. Increasing hinge stiffness allows one to increase the frequency at which wing pitch zero crossing and stroke reversal occur simultaneously.

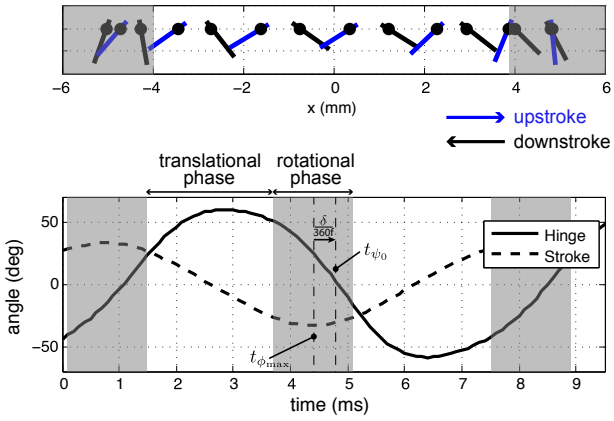

Fig. 3. Wing motion recorded for a stiff hinge flapping at 135Hz and 120V. The top graph illustrates the wing translational motion recorded at 2/3 of its span. The bottom graph shows measured hinge and stroke angles as functions of time. The shaded gray portion represents the rotational phase where stroke angular acceleration is high, and the white portion represents the translational phase.

B. Translational phase

The translational phase refers to the wing motion during midstroke at an approximately constant angle of attack. Dickinson developed a quasi-steady model that accurately describes lift and drag relationships in this phase [6]. In that work, the angle of attack was kept constant during midstroke. This condition cannot be fully reproduced with a passively rotating hinge but, as it will be shown later, can be approximated by focusing the analysis of the hinge angle around the midstroke.

C. Quasi-steady modeling

Experimental characterization of a particular wing requires measurements of lift and drag at different driving frequencies f and stroke amplitudes $\phi_{\max}$. A quasi-steady model can then accurately calculate time-averaged lift and drag based on input kinematics and experimentally fitted force and moment coefficients. In the case of experiments with a passively rotating wing, a moment balance first needs to be solved to predict pitch angle ψ before one can compute the time averaged forces. Hence, it is crucial to find a universal relationship between $\psi_{\max}$, $\phi_{\max}$ and f. More precisely, the minimum angle of attack $\alpha_{\min}$ needs to be predicted based on $\phi_{\max}$ and f.

A quasi-steady model is developed to first compute the mean chordwise center of pressure, R_{cop}, using kinematics measured from experiments. R_{cop} is a function of α and this computed relationship is further used to predict $\alpha_{\min}$ at other stroke and frequency pairs.

R_{cop} is computed by imposing Euler's angular momentum equation:

$$\left.\frac{D\mathbf{L}}{Dt}\right|_{fix} = \left.\frac{D\mathbf{L}}{Dt}\right|_{body} + \boldsymbol{\omega} \times \mathbf{L} \tag{1}$$

where $\mathbf{L}$ is the angular momentum and $\boldsymbol{\omega}$ is the angular velocity of the rigid body. The $\hat{x}_{\mathcal{N}}$ component is:

$$\begin{aligned} &K\alpha - (F_L \cos\alpha + F_D \sin\alpha) R_{\text{cop}} \\ &= I_{xx}\ddot{\alpha} \ + (I_{yy} - I_{zz})\dot{\phi}^2 \cos\psi \sin\psi \end{aligned} \tag{2}$$

where K represents the hinge stiffness, I_{xx} is the effective rotational moment of inertia considering added mass contributions from the surrounding fluid. Before solving for R_{cop}, translational lift and drag are calculated based on measured kinematics:

$$F_i = \frac{1}{2} C_i(\alpha) \rho \int_{x_r}^{x_r+R} (2\pi f)^2 \phi_{\text{max}}^2 r^2 c(r) dr \tag{3}$$

where ρ is the air density, r is the spanwise position, x_r is the wing root location and $c(r)$ is local chord length. Lift and drag coefficients, $C_L(\alpha)$ and $C_D(\alpha)$, are adopted from Dickinson's dynamically scaled measurements [2].

The phase difference between stroke and hinge angles is mostly less than 20° for a wide range of operating points, hence in this quasi-steady model zero relative phase is assumed. The appropriateness of this assumption is discussed in Section IV.

With the experimentally determined parameter R_{cop} , it is possible to solve for α_{min} given new desired operating conditions ϕ_{max}, f, or an alternative K by using Equation (2).

This quasi-steady model greatly simplifies the wing characterization process, since for each wing design only one frequency sweep (to compute R_{cop}) and one voltage sweep (to calculate ϕ_{max} at different driving voltages) are needed. The model should be able to predict α_{min} at any other operating point with any hinge stiffness. The experiments described in this paper are designed to test the reliability and robustness of this characterization method.

III. Experimental setup

The experimental setup consists of a wing driver installed on a custom two-axis force sensor, as illustrated in Figure 4. A high speed camera records the motion of the wing. This section describes the wing driver, the force sensor, the algorithm for motion extraction and wing design and fabrication processes.

A. Wing driver

The wing driver, consisting of a bimorph piezoelectric actuator and a flexure-based transmission, converts the linear displacement of the actuator tip to an angular displacement. The piezoelectric actuator of this wing driver is oversized when compared to the one used on the bee. This pushes the resonance frequency of the wing-piezo system up and allows for a near constant relationship between stroke and voltage below 120Hz. The wing is connected to the transmission by a flexure hinge that allows passive rotation. The wing driver is described in [1].

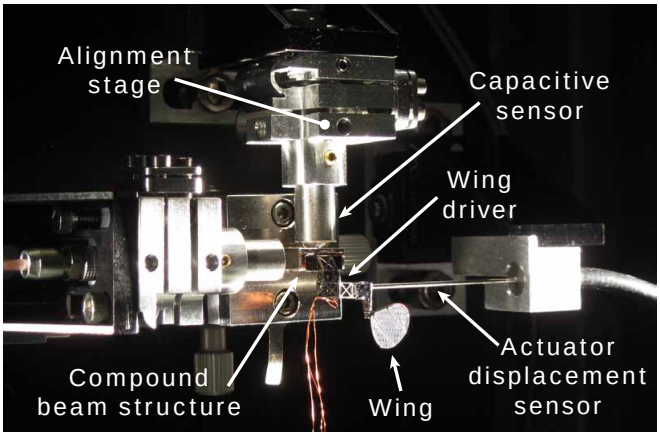

Fig. 4. The experimental setup includes a wing driver installed on a compound beam structure. Capacitive sensors measure the displacement of the structure to calculate the forces along the $\hat{z}_{\mathcal{N}}$ and $\hat{y}_{\mathcal{N}}$ axes.

B. Force measurement

The wing driver is installed on the force sensor input plate ($\hat{y}_{\mathcal{N}} - \hat{z}_{\mathcal{N}}$ plane) similar to the one described in [7]. This sensor consists of four parallel dual cantilever modules arranged in a series-parallel configuration. Each cantilever is 4x4x7mm and made of a single sheet of 150μm Invar that is folded and welded into its final shape. This structure converts a load on the input plate into decoupled, orthogonal displacements along the $\hat{y}_{\mathcal{N}}$ and $\hat{z}_{\mathcal{N}}$ directions. These displacements are measured by two PISeca D-510.021 capacitive sensors. The sensor was statically calibrated by hanging weights, and the resulting sensitivity was found to be -84.6 and 85.5V/N for the $\hat{z}_{\mathcal{N}}$ and $\hat{y}_{\mathcal{N}}$ axis respectively.

The resonant frequency for both axes of a fully loaded sensor was measured to be 510Hz. Force signals are digitized at 5kHz and post-processed with a tenth order zero-phase low pass filter. Only mean forces are presented in this paper. However, time-resolved force measurement is possible up to the sensor resonant frequency.

C. Pitch and Stroke measurement

Wing tracking has traditionally been done manually, or semi-manually where a user fits a 3D model of the wing to video frames [8]–[10]. The experiments described here allow several simplifying assumptions to be made. As the wing is rigid and its motion is limited to flapping in the stroke plane and to hinge rotation, the wing area projected onto the stroke plane will only be a function of the hinge angle. When compared with distance from the wing to the image plane (30cm), the short mean chord length (3mm) makes prospective distortion small.

The wing motion is recorded at 10kHz with a Phantom V7.3 equipped with an AF MICRO Nikkor 200mm f/4 lens. The resulting video is post-processed to extract the hinge and stroke angles. First, the background (i.e. brightest value

throughout the video) is subtracted from the raw image shown in Figure 5 (A). The wing area can then easily be extracted from the white background through thresholding. Using the major axis of the resulting region and two user defined parameters–location of the stroke axis and distance to the wing base–it is then possible to remove the hinge and drive mechanism area. As shown in Figure 5 (C), the major axis orientation of the resulting wing area represents the stroke angle.

Since a model wing has finite leading edge thickness, the area observed by the camera (A_{cam}) is a projection of both the wing (A_{W}) and the leading edge thickness (A_{LE}). The area observed by the camera can be expressed as:

$$A_{\text{cam}} = A_{\text{W}} \sin\psi + A_{\text{LE}} \cos\psi \tag{4}$$

Rearranging the preceding equation and approximating $\cos\psi$ as $\sqrt{(A_{\text{W}}^2 - A_{\text{cam}}^2)}/A_{W_{\max}}$, the absolute value of the hinge angle can be expressed as:

$$\sin|\psi| = \left(A_{\text{cam}} - A_{\text{LE}} \frac{\sqrt{A_{\text{W}}^2 - A_{\text{cam}}^2}}{A_{\text{W}}} \right) \times \frac{1}{A_{\text{W}}} \tag{5}$$

A_{W} can be specified by the user or estimated using the major axis length, R, and the aspect ratio AR, using the relationship $A_{\text{W}} = R^2/AR$. Similarly, A_{LE} can be specified from the smallest area measured during the experiment (i.e. when $\psi \approx 0$).

Finally, the sign of the hinge angle is resolved by comparing the position of the carbon fiber frame's center of area to the wing's center of area along the minor axis.

D. Wing fabrication and design

The wing used in the experiment is made of a carbon fiber frame and polyester membrane manufactured using the Smart Composite Micro structures processes [11]. The wing area (S) was chosen to be 54mm^2 for comparison with previous wing designs.

The wing morphology is based on Ellington's study of insect wing shape parameterization [8]. An insect wing shape can be fully described using a physical scale, a dimensionless function, and two dimensionless numbers. The physical scale is often chosen to be the wing span. The dimensionless function prescribes the leading edge profile as a function of the spanwise coordinate r. The dimensionless parameters are the aspect ratio, the ratio between wing span and mean chord, and the second moment of area, $\hat{r}_2$, that strongly correlates with the center of area $\hat{r}_1$. Ellington showed that most insects have an $\hat{r}_2$ that falls in the range of 0.4 to 0.6, and utilizing a quasi-steady model he further argued that lift is proportional to $\hat{r}_2^2$. In this experiment, $\hat{r}_2$ is set to 0.55. Values of $\hat{r}_2$ higher than 0.6 lead to paddle-shaped wings which experience excessive deformation in flapping experiments.

Lentink studied the aerodynamic effects of rotating rigid plates to understand insect force generation mechanisms during hover [12]. He observed a stable leading edge vortex attached to the leading edge of a rotating plate for local AR smaller than 3. This phenomenon can be characterized by the Coriolis term in the Navier Stokes equation written in a rotating frame, and the effect is analogous to 2-D stall observed in turbo machinery. Therefore, the AR of the current wing is set to 3. This also matches many biological wings [12]. Finally, the leading edge parametrization is adopted from literature to mimic a Drosophila wing [1] .

IV. Results

To examine the robustness of the quasi-steady model proposed in Section II, a wing is driven at various operating points. The corresponding kinematics are recorded for further analysis through techniques described in Section III.

The wing is driven from 80Hz to 145Hz in steps of 5Hz, and the driving voltage is increased from 80V to 130V in units of 10V. Four wing hinges with different stiffness values are built to study the interplay of aerodynamic and elastic hinge torques (Table I). The rotational stiffness k is approximated using the linear elastic deformation equation:

$$k = \frac{Et^3 w}{12l} \tag{6}$$

where E is the Young's modulus of the flexure material, and w , l, and t are flexure width, length, and thickness, respectively. Rotational and translational motions are analyzed separately to identify different force generation mechanisms.

TABLE I
Passive Hinge Stiffnesses

Hinge Label	w (mm)	l (μm)	t (μm)	k (μNm/rad)
Soft	1.25	140	7.5	0.73
Normal	1.25	80	7.5	1.4
Stiff	1.25	45	7.5	2.4
Very Stiff	1.25	155	12.7	3.4

Wing pitch reversal relates to the kinematic parameter δ. If δ is negative, pitch reversal precedes stroke reversal, and favorable circulation develops along the wing boundary layer. As a result, additional lift is generated and drag is reduced. On the other hand, if pitch reversal lags stroke reversal, adverse circulation develops, and lift is reduced and drag is increased. This physical phenomenon was first identified by Dickinson using independent pitch and stroke control [2]. Sane et Al [13] also reported advanced rotation facilitates wake capture, which is beneficial towards lift generation. In this passive rotation experiment, the relationship between pitch reversal and stroke reversal is observed to vary with frequency. As shown in Figure 6, advanced pitch reversal is observed at low frequencies and delayed pitch reversal is observed at high frequencies. This observation shows that the hinge spring torque dominates the aerodynamic and inertial torque contributions at low frequencies, therefore a stiffer hinge design is beneficial to lift enhancement during the rotational phase, as seen in Figure 7. Our result confirms that given similar stroke and pitch motion advanced pitching increases mean lift.

In the translational phase, maximum lift is generated when α_{min} equals $45°$, (typically at midstroke). To predict α_{min} at a particular operating point, it is crucial to analyze the

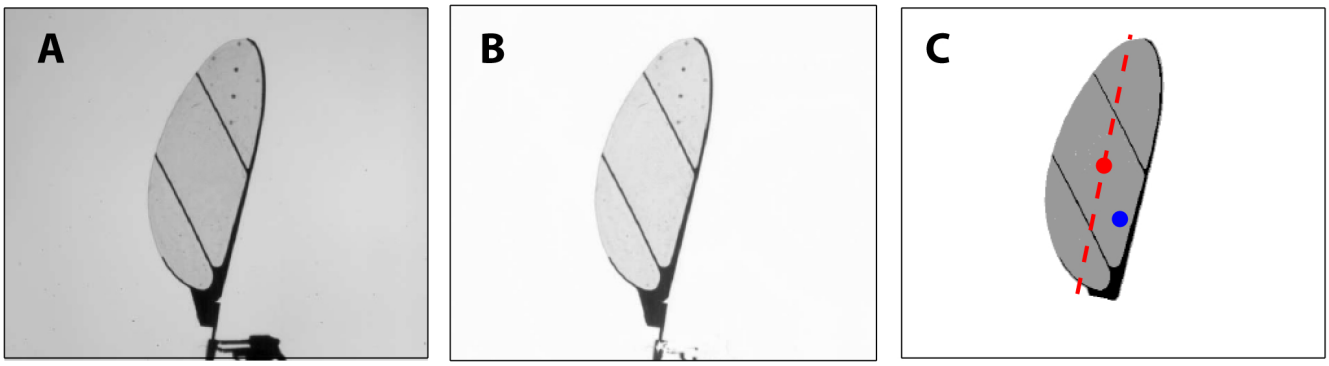

Fig. 5. Image extraction process. First the background is extracted from the original image (**A**) to produce image **B**. Different gray levels are used to differentiate the carbon fiber frame (black region in **C**) from the wing area (gray region in **C**). Also illustrated are the centroid of both regions (red = wing area, blue = carbon fiber frame) and the major axis of the wing area (red dashed line).

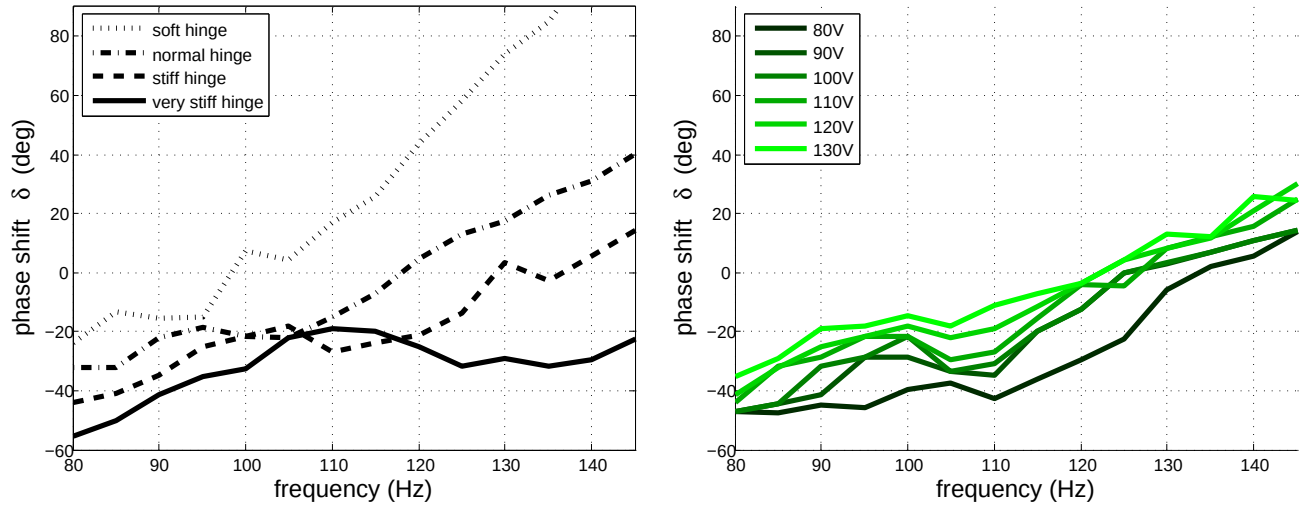

Fig. 6. Relative phase shift δ as a function of frequency for changing hinge stiffnesses (left) and changing driving voltage (right). The plot on the left shows δ versus f for different hinge stiffnesses, where the driving voltage is fixed at 120V. The plot on the right shows experiments with a stiff hinge and varying driving voltage from 80V to 130V. Advanced wing pitch reversal occurs at low frequencies and stroke amplitudes, which suggests the elastic hinge torque dominates aerodynamic and inertia contributions for low stroke velocity. Increased hinge stiffness further enhances rotational circulation to increase lift and reduce drag. However, a very stiff hinge reduces $\psi_{\max}$ so that the desired $\alpha_{\min}$ cannot be achieved. Small hinge motion leads to excessive loading on the wing driver and $\phi_{\max}$ is reduced. While a stiff hinge allows advanced pitch reversal, it reduces performance during the translational phase. For a fixed hinge stiffness, δ increases as drive voltage increases (right). Hence, to achieve optimal performance, the wing driver should operate at maximum voltage in combination with a stiff hinge.

relationship between three kinematic parameters: $\phi_{\max}$, $\psi_{\max}$ and $\alpha_{\min}$. Figure 8 (left) shows the relationship between $\psi_{\max}$ (equivalently, $\pi/2 - \alpha_{\min}$) and $\phi_{\max}$ at various testing conditions. Each curve on the plot represents a discrete frequency sweep (80Hz to 145Hz) at a fixed drive voltage. Figure 8 (right) shows the same data by plotting hinge angle as a function of wing tip velocity. Note that all curves from Figure 8 (left) overlap in Figure 8 (right) suggesting a universal relationship between maximum stroke velocity and maximum hinge angle. This observation supports the assumption that the effect of δ on translational lift at midstroke is small.

Using the quasi-steady model derived in Section II, R_{cop} is computed as a function of α. Each curve in Figure 9 shows this relationship while driving the wing at a fixed voltage at the same time discretely varying the frequency. This measured relationship between angle of attack and center of pressure is similar to that detailed in [6], in which Dickson measured center of pressure as a function of angle of attack for a flat plate translating at constant veolcity. Note that in both cases the center of pressure is not located at quarter chord, since the classical quarter chord derivation is based on irrotational thin airfoil theory without flow seperation. This relationship is purely geometric and hence all curves should completely overlap. The discrepancy observed may be due to the effect of the small but non-zero phase δ.

The center of pressure relationship can be used to further predict changes to kinematic parameters as hinge stiffness varies. Accurately predicting kinematic parameters $\alpha_{\min}$, $\phi_{\max}$, and f at specific operating points for different hinge

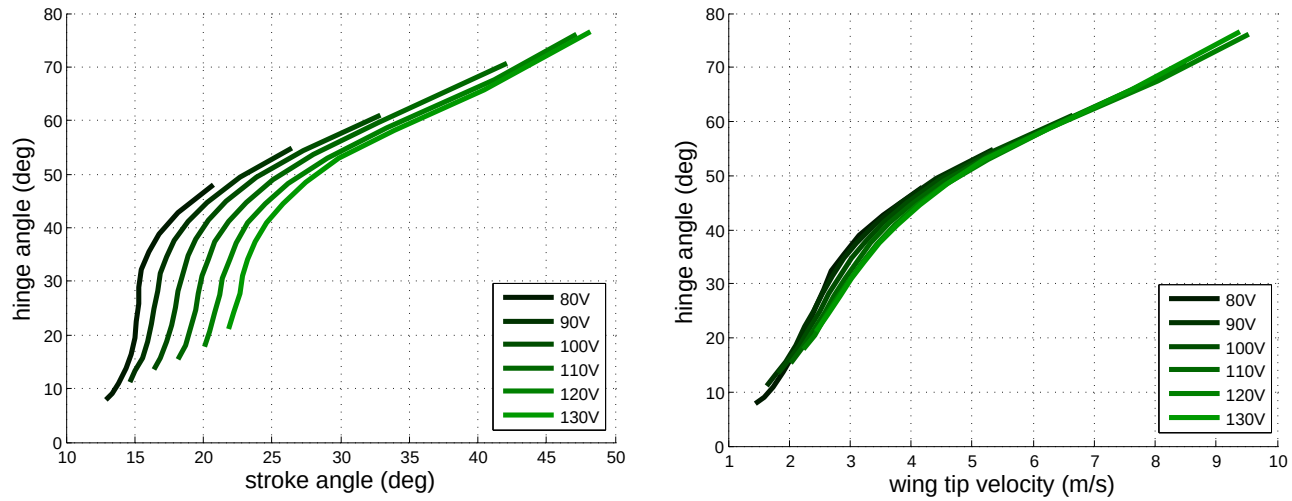

Fig. 8. Maximum hinge angle versus maximum stroke angle (left) and maximum hinge angle versus maximum stroke velocity (right). Individual curves on the left are compressed into a universal relationship between maximum stroke velocity and hinge angle. The curve on the right can be used to predict the curves on the left by running a frequency sweep and a voltage sweep. The original plot (left) requires 84 experiments whereas the reconstruction method only uses 19 experiments. The agreement in hinge angle between reconstructions and experiments is accurate to within 3 degrees.

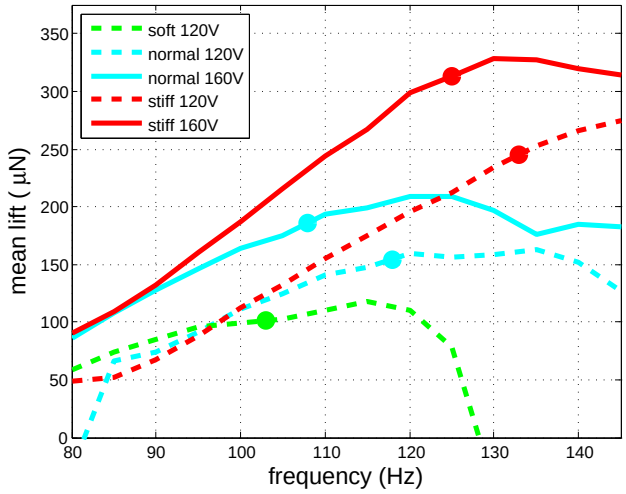

Fig. 7. Mean lift versus frequency with changing hinge stiffnesses and driving voltages. Comparison between stiff, normal and soft hinges driven at 120V shows that increase of hinge stiffness increases time-averaged lift. This lift increase is largely due to increase in rotational circulation.The maximum stroke angle for experiments below 120Hz remains roughly constant. Comparison between a particular hinge (normal or stiff) driven at 120V and 160V shows that increased driving voltage increases the time-averaged lift. This is largely due to the increase in stroke amplitude $\phi_{\max}$. The dot on each curve marks the critical frequency at which δ becomes positive. Rotational circulation becomes adverse to lift generation at frequencies higher than the critical frequency.

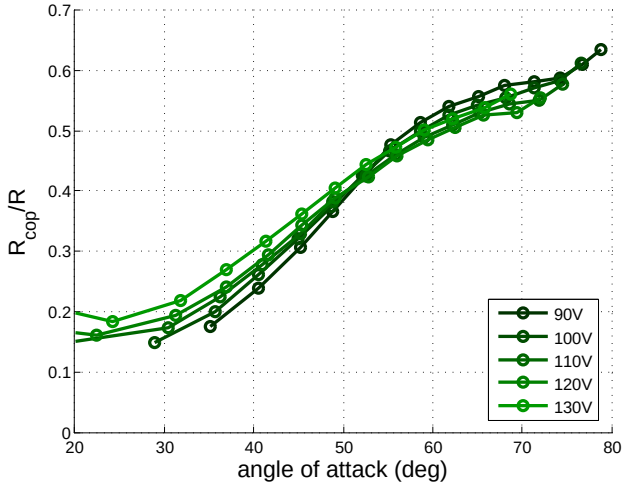

Fig. 9. Center of pressure at maximum hinge angle versus angle of attack. This was calculated using the quasi-steady model from [2] and is mostly independent of frequency. The y-axis shows center of pressure scaled by mean chord length. At large α, we expect R_{cop}/R to be in vicinity of 0.5. This computed relationship varies slightly for different driving voltages, and this discrepancy is due to the non-zero relative phase shift δ.

stiffnesses reduces the number of experiments needed for wing characterization. Figure 10 shows examples of such predictions. Maximum stroke velocities and maximum hinge angles are measured for the wing with a stiff hinge. The quasi-steady model further predicts stroke velocity and hinge angle relationships for varying hinge stiffnesses. Experiments with the other hinge designs (soft, normal and very stiff) are later taken to examine the accuracy of this method. While the predictions for the normal and the stiff hinge show good agreement with experiments, the prediction for the soft hinge is inaccurate at high stroke velocity. This discrepancy can be understood by observing the large δ for the soft hinge design at high flapping frequencies as shown in Figure 6. This quasi-steady model fails at large δ since the maximum stroke velocity does not coincide with the maximum hinge angle. Overall, the quasi-steady model does not require extra fitting parameters, hence the agreement between prediction and actual measurements confirms its validity.

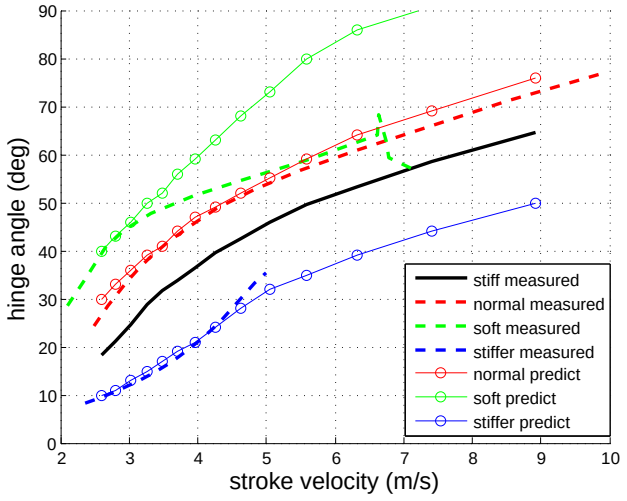

Fig. 10. Hinge angle prediction as function of wing tip velocity at different hinge stiffnesses. This relationship for the stiff hinge is measured to compute R_{cop} as a function of α. Utilizing the R_{cop} function, the hinge angle function is predicted for the soft, normal and very stiff hinge. The predictions for normal and very stiff hinge show good agreements with measurements. However, as shown by the blue dotted line, wing tip velocity of the wing with the very stiff hinge does not exceed $5m/s$. Very small hinge motion leads to large drag that limits ϕ_{max}. The quasi-steady model does not consider actuator limitations. Further, as shown by the green lines, the prediction for the wing kinematics of the soft hinge deviates from measurements at high stroke velocity. This can be explained by large δ shown in Figure 6. The difference between quasi-steady prediction of ψ_{max} and measurements is always smaller than 6° for $\delta < 40^\circ$.

This characterization method can be very useful for wing shape optimization studies. Usually, mechanical limitations (e.g. actuator saturation or failure, flexure failure) of micro-air vehicles restrict wing operational ranges, thus it is important to choose an appropriate wing hinge stiffness that leads to optimal flapping kinematics. Given a specific driving frequency and voltage, an appropriate hinge stiffness can be chosen to achieve maximum translational lift ($\alpha = 45^\circ$) using this model and method.

V. Conclusions and Future Work

In this study, a quasi-steady model based on a torque balance about a compliant hinge is proposed to describe the kinematics of a passively rotating insect-scale wing. The model is developed into a robust wing characterization method that predicts α_{min} given K, ϕ_{max}, and f. Flapping experiments at different operating points show an accuracy within 6° for $\delta < 40^\circ$ (Figure 10). This suggests the previous "brute force" wing performance characterization method can be greatly simplified, as the number of flapping experiments required is reduced by a factor of four (caption of Figure 8).

Since the predicted kinematic parameters closely relate to time-averaged lift and drag measurements, the quasi-steady method can be also used to improve wing performance. At a particular operating point, the model computes the hinge stiffness that leads to optimal translational motion, which directly leads to maximum lift generation. In contrast to the previous "trial and error" approach for hinge stiffness design, the quasi-steady model calculates optimal stiffness for a particular wing operated at a specific driving voltage and flapping frequency.

In addition, the experiments demonstrate that a stiffer hinge advances pitch reversal relative to stroke reversal. This observation suggests that passive hinge design can also generate rotational circulation, which leads to lift enhancement and drag reduction. Ensuing studies should focus on unsteady force generation mechanisms during pitch reversal and examine the effect of δ on translational motion. This effect should reduce the aerodynamic center computation discrepancy shown in Figure 9. Finally, equipped with the quasi-steady model for both passive wing pitch reversal and translational motion, numerical and experimental studies can focus on leading edge wing shape optimization.

VI. Acknowledgement

This work was partially supported by the National Science Foundation (award number CCF-0926148), and the Wyss Institute for Biologically Inspired Engineering. Any opinions, findings, and conclusions or recommendations expressed in this material are those of the authors and do not necessarily reflect the views of the National Science Foundation.

References

[1] J. P. Whitney, "Design and performance of insect-scale flapping-wing vehicles," Ph.D. dissertation, Harvard University, 2012.

[2] M. H. Dickinson, F.-O. Lehmann, and S. P. Sane, "Wing rotation and the aerodynamic basis of insect flight," *Science*, vol. 284, no. 5422, pp. 1954–1960, 1999.

[3] A. R. ENNOS, "The inertial cause of wing rotation in diptera," *Journal of experimental biology*, vol. 140, no. 1, pp. 161–169, 1988.

[4] A. J. Bergou, S. Xu, and Z. Wang, "Passive wing pitch reversal in insect flight," *Journal of Fluid Mechanics*, vol. 591, no. 1, pp. 321–337, 2007.

[5] J. Whitney and R. Wood, "Aeromechanics of passive rotation in flapping flight," *Journal of Fluid Mechanics*, vol. 660, no. 1, pp. 197–220, 2010.

[6] W. B. Dickson, A. D. Straw, and M. H. Dickinson, "Integrative model of drosophila flight," *AIAA journal*, vol. 46, no. 9, pp. 2150–2164, 2008.

[7] R. Wood, K. Cho, and K. Hoffman, "A novel multi-axis force sensor for microrobotics applications," *Smart Materials and Structures*, vol. 18, no. 12, p. 125002, 2009.

[8] C. Ellington and C. Ellington, "The aerodynamics of hovering insect flight the quasi-steady analysis," *Philosophical Transactions of the Royal Society of London. B, Biological Sciences*, vol. 305, no. 1122, pp. 1–15, 1984.

[9] S. N. Fry, R. Sayaman, and M. H. Dickinson, "The aerodynamics of free-flight maneuvers in drosophila," *Science*, vol. 300, no. 5618, pp. 495–498, 2003.

[10] Y. Liu and M. Sun, "Wing kinematics measurement and aerodynamics of hovering droneflies," *Journal of Experimental Biology*, vol. 211, no. 13, pp. 2014–2025, 2008.

[11] R. Wood, S. Avadhanula, R. Sahai, E. Steltz, and R. Fearing, "Microrobot design using fiber reinforced composites," *Journal of Mechanical Design*, vol. 130, p. 052304, 2008.

[12] D. Lentink and M. H. Dickinson, "Rotational accelerations stabilize leading edge vortices on revolving fly wings," *Journal of Experimental Biology*, vol. 212, no. 16, pp. 2705–2719, 2009.

[13] S. P. Sane and M. H. Dickinson, "The control of flight force by a flapping wing: lift and drag production," *Journal of experimental biology*, vol. 204, no. 15, pp. 2607–2626, 2001.